Phase-space structure of cold dark matter haloes inside splashback: multistream flows and self-similar solution

Hiromu Sugiura, Takahiro Nishimichi, Yann Rasera, Atsushi Taruya

Monthly Notices
of the
ROYAL ASTRONOMICAL SOCIETY

MNRAS **493,** 2765–2781 (2020)
Advance Access publication 2020 February 14

doi:10.1093/mnras/staa413

Phase-space structure of cold dark matter haloes inside splashback: multistream flows and self-similar solution.

Hiromu Sugiura,[1]★ Takahiro Nishimichi [2,3] Yann Rasera[4] and Atsushi Taruya [2,3]

[1]*Department of Physics, Kyoto University, Kyoto 606-8502, Japan*
[2]*Center for Gravitational Physics, Yukawa Institute for Theoretical Physics, Kyoto University, Kyoto 606-8502, Japan*
[3]*Kavli Institute for the Physics and Mathematics of the Universe (WPI), The University of Tokyo Institutes for Advanced Study, The University of Tokyo, 5-1-5 Kashiwanoha, Kashiwa, Chiba 277-8583, Japan*
[4]*LUTH, Observatoire de Paris, PSL Research University, CNRS, Université Paris Diderot, Sorbonne Paris Cité, 5 place Jules Janssen, F-92195 Meudon, France*

Accepted 2020 February 5. Received 2020 January 24; in original form 2019 December 6

ABSTRACT

Using the motion of accreting particles on to haloes in cosmological *N*-body simulations, we study the radial phase-space structures of cold dark matter (CDM) haloes. In CDM cosmology, formation of virialized haloes generically produces radial caustics, followed by multistream flows of accreted dark matter inside the haloes. In particular, the radius of the outermost caustic called the splashback radius exhibits a sharp drop in the slope of the density profile. Here, we focus on the multistream structure of CDM haloes inside the splashback radius. To analyse this, we use and extend the SPARTA algorithm developed by Diemer. By tracking the particle trajectories accreting on to the haloes, we count their number of apocentre passages, which is then used to reveal the multistream flows of the dark matter particles. The resultant multistream structure in radial phase space is compared with the prediction of the self-similar solution by Fillmore & Goldreich for each halo. We find that ∼30 per cent of the simulated haloes satisfy our criteria to be regarded as being well fitted to the self-similar solution. The fitting parameters in the self-similar solution characterize physical properties of the haloes, including the mass accretion rate and the size of the outermost caustic (i.e. the splashback radius). We discuss in detail the correlation of these fitting parameters and other measures directly extracted from the *N*-body simulation.

Key words: methods: numerical – dark matter – cosmology: theory.

1 INTRODUCTION

The concordant cosmological model, i.e. lambda cold dark matter (ΛCDM) model, provides a simple picture of both the cosmic expansion and structure formation in the Universe with a minimal set of model parameters. The model consistently explains multiple cosmological observations, and the model parameters are measured precisely with the statistical error of a few per cent level by the cosmic microwave background experiment (Planck Collaboration VI 2018). According to this model, the large-scale matter inhomogeneities have evolved under the influence of gravity and cosmic expansion, starting with tiny density fluctuations that would have been generated in the early universe. An important ingredient of late-time structure formation driven by gravity is the cold dark matter (CDM), which amounts to more than 80 per cent of the matter components (Blumenthal, Pagels & Primack 1982; Bond, Szalay & Turner 1982; Peebles 1982). As it is named, the CDM was initially cold with negligibly small velocity dispersion, and behaved like dust fluid at the very early stage of structure formation. Later, due to the attractive force of gravity, the CDM gradually accretes into overdense regions, and matter concentration grows. When the amplitude of the density contrast exceeds unity, the growth of fluctuations becomes non-linear, finally ending up with the formation of self-gravitating bounded objects called dark matter haloes through the collapse and virialization (Binney & Tremaine 2008). Since a sufficient amount of baryon has been accumulated by the gravitational potential well of dark matter after the recombination epoch, the dark matter halo is an ideal site of galaxy and star formation, and thus observationally important to probe the structure formation and cosmology.

Within the CDM paradigm, there have been numerous works to characterize the kinematical, dynamical, and statistical properties of dark matter haloes. One important feature found in numerical simulations but not yet clearly understood is the cuspy density profile called the NFW profile (Navarro, Frenk & White 1996).

★ E-mail: sugiura@tap.scphys.kyoto-u.ac.jp

Unlike naive theoretical expectations, the radially averaged density profile $\rho(r)$ near the halo centre exhibits a shallow cusp, whose logarithmic slope, defined by $\mathrm{d}\log\rho/\mathrm{d}\ln r$, is larger than -2, mostly independent of cosmology and the size of haloes. Another striking feature, also found in the cosmological *N*-body simulations, is the power-law nature of the pseudo-phase-space density profile defined by $\rho(r)/\sigma^3(r)$, with $\sigma(r)$ being the velocity dispersion (Taylor & Navarro 2001; Ludlow et al. 2010; Navarro et al. 2010). The slope found in the simulations closely matches the prediction of the Bertschinger's secondary infall model (Bertschinger 1985), suggesting that the structure of haloes is built up with continuous accretion flow and mergers. Yet, recalling the fact that the haloes are not fully spherical but generically asymmetric with sizable amount of substructures, how such a simple picture can reconcile with the actual halo formation processes still remains unclear. Viewing the halo formation from the viewpoint of collisionless self-gravitating system, CDM haloes generally have some memories of the initial condition, and due to its cold nature, unique and characteristic features appear manifest, in particular, in phase space. In fact, generic properties of the CDM halo mentioned above are linked with each other, and one expects that these are originated from the phase-space dynamics of the CDM haloes. In this respect, the structural and statistical properties of the haloes in phase space are worth investigating, and there are thus numerous works along the line of this (e.g. Drakos, Taylor & Benson 2017; Halle, Colombi & Peirani 2019, for recent works). Also, a quantitative phase-space study would serve as a clue to discriminate CDM from non-standard dark matter scenarios, and in combination with observations, it may help to clarify the nature of dark matter (e.g. Sikivie, Tkachev & Wang 1997).

To be more precise, the CDM inside haloes is expected to have underwent shell crossing during the accretion, and the velocity at a given position gets multivalued. On the other hand, the regions outside haloes exhibit a single-stream flow, for which the velocity of accreting matter is uniquely determined as a function of position. Importantly, the collisionless and Hamiltonian nature of the system ensures that the phase-space density is conserved, and its topological structure remains unchanged. Thus, the single-stream flow should smoothly be connected to the multistream flow. Recently, Diemer & Kravtsov (2014) pointed out that there is a significant deviation of the density profile from the NFW profile at the outskirt of haloes, and this can happen exactly at the boundary between single- and multistream flow regions (Adhikari, Dalal & Chamberlain 2014). In *N*-body simulation, the location of this boundary corresponds to the first apocentre of the accreting dark matter particles, particularly referred to as the splashback radius. Because of its clear manifestation, the observational prospects and the theoretical understanding of the splashback feature as a unique signature of the CDM paradigm have attracted much attention (More, Diemer & Kravtsov 2015; More et al. 2016a,b; Shi 2016; Busch & White 2017; Diemer 2017; Diemer et al. 2017; Adhikari et al. 2018; Chang et al. 2018; Okumura et al. 2018).

It is theoretically expected that the splashback feature in the radial density profile appears more prominent in spherically symmetric haloes, for which several self-similar solutions are known in the Einstein–de Sitter universe (e.g. Fillmore & Goldreich 1984; Bertschinger 1985; White & Zaritsky 1992; Ryden 1993; Zukin & Bertschinger 2010; Lithwick & Dalal 2011; Vogelsberger, Mohayaee & White 2011; Alard 2013). Because of the exact spherical symmetry, the density profile of self-similar solution exhibits apparent divergences called caustics at the apocentres of each flow of accreting matter. The outermost caustic particularly shows the most notable feature, and its location exactly corresponds to the splashback radius (Adhikari et al. 2014). Shi (2016) used the self-similar solution by Fillmore & Goldreich (1984) to give an analytical prediction of the splashback radius, and Diemer et al. (2017) found good agreement with numerical simulations. This suggests that the self-similar solution may capture the overall trends in the dynamics of accreting material on to CDM haloes in simulations, and possibly those in the real universe if the CDM scenario is true, although it is very hard to imagine that spherically symmetric and isolated halo is realized in reality. In fact, even when starting from a nearly spherically symmetric initial condition, non-sphericity is rapidly developed due to the so-called radial orbit instability (e.g. Binney & Tremaine 2008), and a deviation from the top-hat spherical collapse model is significant (Suto et al. 2016a). The resultant halo exhibits an elongated triaxial shape (e.g. Jing & Suto 2002; Suto et al. 2016b), rather different from the prediction of the self-similar solution (e.g. MacMillan, Widrow & Henriksen 2006). Nevertheless, the growth of haloes and the evolved density profile are found to match the prediction of the self-similar solution. There are also several works advocating that taking spherical average, the phase-space structures of haloes in *N*-body simulations resemble the spherical self-similar solutions (e.g. Bertschinger & Gelb 1991; Henriksen & Widrow 1997; Mohayaee et al. 2006; Vogelsberger et al. 2009; Vogelsberger & White 2011; Dolag, Dolgov & Tkachev 2013). In these respects, it is still interesting to further clarify the similarities and differences between the self-similar solution and the full dynamics in *N*-body simulations in more quantitative manner. In particular, little work has focused on the multistream structure of CDM haloes, and a detailed analysis from the phase space point of view has not yet been made.

In this paper, we compare the phase-space structure of haloes in a cosmological *N*-body simulation with those predicted from the self-similar solution, and try to clarify to what extent the multistream features agree between the two descriptions. Although the internal structures of haloes are driven by the collisionless gravitational dynamics and thus the memory of initial condition should still remain preserved to some extent, generic properties of haloes, including the universality in the density profile or the pseudo-phase-space density scaling, are built up along the halo formation processes. In this respect, a phase-space comparison with self-similar solution would give a useful guideline or hint to understand how the generic features emerge and what environment-dependent features remain especially in the internal halo structures. In doing so, the statistical analysis using a large number of haloes is important, and in this paper, we will make a detailed comparison of radial phase-space structures with self-similar solution for massive haloes found in an *N*-body simulation. A crucial point in this work is to extract different streams in each halo to reveal the multistreaming structure. For this purpose, we adopt and extend the SPARTA algorithm by Diemer (2017). In short, using a number of output data at different redshifts, we keep track of the trajectories of dark matter particles around the haloes, and count the number of apocentre passages for each dark matter particle. Sorting out all the particles around a halo with the number of apocentre passages, we can visualize, in phase space, each stream line of multistream flows inside the halo.

This paper is organized as follows. In Section 2, we present a brief review of the spherical self-similar solutions. Section 3 describes the method that we adopt to analyse the dark matter haloes identified in an *N*-body simulation. We show our results in Section 4 and discuss its implication in Section 5. Our conclusion from the analysis and further discussions are finally presented in Section 6.

2 SPHERICAL SELF-SIMILAR SOLUTIONS

In this section, we present a brief review of the self-similar solution described by Fillmore & Goldreich (1984) and Bertschinger (1985).

Consider a spherically symmetric density contrast in the Einstein–de Sitter universe, with surrounding materials stationary accreting towards the centre. The dynamics of such a system is described by a collection of spherical shells moving radially. Although all the shells move outward in the radial direction according to the Hubble–Lemaître law at first, as increasing the central density due to the gravitational growth, the motion of surrounding shells ceases to follow the cosmic expansion, and start to infall into the central region (e.g. Gunn & Gott 1972; Gunn 1977; Peebles 1980). The time of this critical point is referred to as the turnaround time $t_{\rm ta}$, and the physical size/radius of the shell at that time is called the turnaround radius $r_{\rm ta}$, which is given as the function of $t_{\rm ta}$. Since each shell has different turnaround time, the properties of the system can be characterized by a family of the shell radii parametrized by $t_{\rm ta}$, hence we denote it by $r(t, t_{\rm ta})$.

Imposing the self-similarity, the function $r(t, t_{\rm ta})$ can be written in the form as

$$r(t, t_{\rm ta}) = r_{\rm ta}(t_{\rm ta})\lambda(t/t_{\rm ta}), \tag{1}$$

where λ is a dimensionless quantity. The functional form of $r_{\rm ta}(t_{\rm ta})$ depends on the initial condition. Assuming a power law for the initial density contrast given by $\delta_{\rm i}\propto r^{-3/s}$, we have

$$r_{\rm ta}(t_{\rm ta}) \propto t_{\rm ta}^{\beta}, \quad \beta = \frac{2}{3} + \frac{2}{9}s. \tag{2}$$

The parameter, s, introduced above is related to the mass accretion rate, and it is expressed as $s = {\rm dln}\, M_{\rm ta}/{\rm dln}\, a$, where $M_{\rm ta}$ is the enclosed mass within $r_{\rm ta}$ at the turnaround epoch $t_{\rm ta}$ and $a\propto t^{2/3}$ is the scale factor of the Universe (Adhikari et al. 2014; Shi 2016).[1] Note that this parameter s fully determines the asymptotic inner slope of the density profile, $\gamma \equiv {\rm dln}\,\rho/{\rm dln}\, r$, through

$$\gamma = -\frac{9}{3+s} \ \text{ for } s \le \frac{3}{2}, \quad \gamma = -2 \ \text{ for } s \ge \frac{3}{2}. \tag{3}$$

With these set-ups, the solution in the special case with $s = 1$ corresponds to the self-similar solution of the collisionless secondary infall by Bertschinger (1985).

In equation (1), the function $\lambda(\tau)$ is obtained by solving the equation of motion for shells

$$\frac{{\rm d}^2 r}{{\rm d}t^2} = -\frac{GM}{r^2}, \tag{4}$$

where M is the mass enclosed by the shell. Under the assumption of self-similarity, this equation is reduced to the non-dimensional form (Fillmore & Goldreich 1984)

$$\frac{{\rm d}^2\lambda}{{\rm d}\tau^2} = -\frac{\pi^2}{8}\frac{\tau^{2s/3}}{\lambda^2}\mathcal{M}(\lambda/\tau^{\beta}). \tag{5}$$

Here, the function $\mathcal{M}(\xi)$ is a non-dimensional mass variable corresponding to the enclosed mass M in equation (4), i.e. the mass profile normalized by the turnaround mass, given in the integral form

$$\mathcal{M}(\xi) = \frac{2s}{3}\int_1^{\infty} \Theta\left[\xi - \frac{\lambda(\tau')}{\tau'^{\beta}}\right]\frac{{\rm d}\tau'}{\tau'^{1+2s/3}}, \tag{6}$$

where $\Theta(x)$ is the Heaviside step function. Thus, equation (5) is the integro–differential equation, which has to be solved numerically based on an iterative method. That is, first we take an initial guess for the mass profile and solve the equation of motion. We set $\mathcal{M}(\xi) = \xi$ as our simple initial guess. The solution for λ obtained at the first trial is then used to estimate $\mathcal{M}$ through equation (6), which will be next used to solve equation (5) in the second trial. We repeat this procedure until the radial positions of the first five apocentres (i.e. the position at which ${\rm d}\lambda/{\rm d}\tau = 0$ is satisfied) are converged well within the accuracy of 0.1 per cent. In solving equation (5) in practice, we need to introduce a small angular momentum to avoid the singular behaviour at $\lambda = 0$ (Bertschinger 1985; Mohayaee & Shandarin 2006). This alters the solution near the centre, and we adjust the angular momentum so that its impacts on the locations of first five apocentres are less than 0.1 per cent. We calculated the self-similar solutions in the parameter range $0.1 \le s \le 9$.

The numerical solution of λ, given as a function of $\tau = t/t_{\rm ta}$, describes the motion of a single shell specified by a value of $t_{\rm ta}$. If we instead fix t and draw λ as a function of $t_{\rm ta}$, it can give a snapshot of the distribution of a family of shells parametrized by $t_{\rm ta}$. In other words, at a given time t, the function $r(t, t_{\rm ta})$ and its time derivative $\partial r/\partial t$, plotted as function of $t_{\rm ta}$, forms radial phase-space trajectories for a collection of shells

$$\left(r(t, t_{\rm ta}),\ \frac{\partial r}{\partial t}(t, t_{\rm ta})\right)_{t_{\rm ta}\in(0,t]} = \left(r_{\rm ta}(t)\tau^{-\beta}\lambda(\tau),\ \frac{r_{\rm ta}(t)}{t}\tau^{1-\beta}\frac{{\rm d}\lambda}{{\rm d}\tau}(\tau)\right)_{\tau\in[1,\infty)}. \tag{7}$$

Fig. 1 shows the snapshots of the self-similar solution for specific values of the parameter, $s = 1$ (left), 2 (middle), and 3 (right). Here, the horizontal axis in each panel is normalized by the radius R_{200}, within which the mean overdensity exceeds 200 times the background mass density (or equivalently the critical density in the Einstein–de Sitter universe), and the vertical axis represents the dimensionless velocity, i.e. $\tau^{1-\beta}({\rm d}\lambda/{\rm d}\tau)$. The size of haloes is supposed to be characterized by the radius R_{200} roughly corresponding to the virial radius, but the actual size/region where the multistream flow can be extended out to a larger radius depending on the mass accretion rate parameter s. Overall, the size of the multistream region tends to get compressed as increasing s. In this respect, the so-called splashback radius, $r_{\rm sp}$, as indicated by the vertical dotted line in Fig. 1, provides a more appropriate definition of the size of a halo. Here, the location of the splashback radius is determined by the outermost location that satisfies the condition $(\partial r/\partial t)_{r_{\rm sp}} = 0$. Note that in general, the location of the outermost caustic, defined by ${\rm d}v/{\rm d}r = 0$, does not precisely coincide with the splashback radius defined here, although several works have used the outermost caustic as the boundary of a halo, which can be clearly seen from the sudden change in the slope of the radial density profile (e.g. Diemer & Kravtsov 2014; More et al. 2015). The reason why the locations of the caustic and the apocentre are different in phase space basically follows from the stationary mass accretion. That is, looking at the motion of shells, we see that the apocentre radius for each shell becomes gradually increasing in time $t_{\rm ta}$ due to the continuous mass growth at the centre. Then, viewing a collection of shells in phase space at a given time t, we can find a small segment in the flow line that have a positive radial velocity, i.e. the shells that have not yet experienced an apocentre passage, but have a radial coordinate larger than the preceding shell that has just undergone an apocentre passage ($v = 0$), i.e. the splashback radius. In general, the radial location of the caustic tends to be larger than that of the apocentre in the presence of mass accretion.

[1] In Fillmore & Goldreich (1984), they use $\epsilon = 1/s$, instead of s.

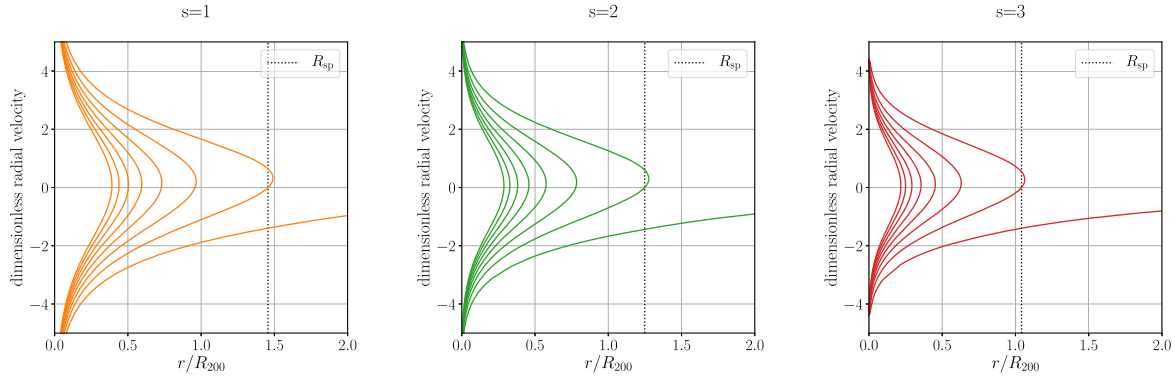

Figure 1. Phase-space portraits of the self-similar solution for $s = 1$ (left), 2 (middle), and 3 (right). The horizontal axis represents the radial position normalized by the radius R_{200}, at which the mean overdensity of the halo reaches 200 times the background mass density. The vertical axis means the dimensionless velocity, $\tau^{1-\beta}(\mathrm{d}\lambda/\mathrm{d}\tau)$. The plot shows the trajectories up to the seventh apocentre passages. The vertical dotted lines indicate the splashback radius $R_{\rm sp}$ at which the trajectory crosses the zero-velocity line.

Table 1. Summary of the cosmological parameters used in this paper. $\Omega_{\rm m}$ is the matter density, $\Omega_{\rm r}$ is the radiation density, $\Omega_{\rm b}$ is the baryon density, σ_8 and n_s give the normalization and slope of the primordial matter power spectrum, and h is the hubble parameter.

$\Omega_{\rm m}$	$\Omega_{\rm r}$	$\Omega_{\rm b}$	σ_8	$n_{\rm s}$	h
0.99992	0.00008	0.04356	0.801	0.963	0.72

3 METHOD

3.1 *N*-body simulation

We performed an *N*-body simulation with $N = (512)^3$ particles distributed in a $(164.0625\ h^{-1}\mathrm{Mpc})^3$ volume with an (almost) Einstein–de Sitter cosmology. The choice of this cosmology is driven by the secondary infall model that is only valid in Einstein–de Sitter cosmology. We, however, prefer to keep a radiation component so that our early universe calculation with the CAMB code (Lewis, Challinor & Lasenby 2000) remains accurate. This component is completely negligible in the late universe of interest in this paper ($z < 2$). The cosmological parameters are given in Table 1.

We use the same simulation set-up as in Blot et al. (2015) focusing on a single realization. Initial conditions are generated at an initial redshift of $z_{\rm i} = 40$ with MPGRAFIC (Prunet et al. 2008) and assuming second-order Lagrangian perturbation theory (2LPT) for the displacement. The dynamical evolution of dark matter particles is calculated with RAMSES (Teyssier 2002). In order to trace the motions of particles, it is necessary to store enough snapshots of the simulation (Diemer 2017). We stored 60 snapshots between redshifts 1.43 and 0, and labelled them by n in ascending order of time. The snapshots are regularly spaced in expansion factor a with $\delta a \approx 0.01$. The snapshot $n = 40$ corresponds to $a = 0.411$ or $z = 1.43$ and the snapshot $n = 99$ corresponds to $a = 1$ or $z = 0$.

From these snapshots, we compute the density on a grid with 1024^3 elements using a Cloud-In-Cell assignment scheme (CIC). The density at the location of the particles ρ_i is linearly interpolated from the density in the grid (i.e. using an inverse CIC scheme). We detect haloes at $z = 0$ (only) with a parallel version (called pSOD) of the spherical overdensity (SO) halo finder algorithm (Lacey & Cole 1994). The centre of haloes is defined as the most dense particle (which is close to the minimum of potential). A sphere is then grown around this centre until the overdensity $\Delta_{\rm m} = 200$ (relative to the mean matter density in the universe) is reached. We found 11 296 haloes. After all haloes are detected, we obtain a list of halo centres at $z = 0$. Note that the size R_{200} and mass M_{200} of the SO haloes as well as the location of SO haloes at higher redshift do not play a role in the tracking procedure described below: this procedure only depends on the location of the centre and the orbits of the particles around the centre. This is in contrast from other tracking procedures (such as in Diemer 2017) where the tracking can start only after halo finders have been run on all snapshots.

3.2 Tracking haloes and particles

In order to study the radial phase-space structure for each halo, we analyse snapshots densely sampled in time to keep track of the trajectories of dark matter particles. We, in particular, classify the trajectory of each dark matter particle by the number of apocentre passages experienced before $z = 0$. To do so, we first need to identify the centre of each halo at each snapshot, and then define the distance to each dark matter particle from the halo centre, as well as the velocity of dark matter subtracting the bulk motion of the halo at the centre. In Section 3.2.1, we present the prescription to determine the location of the halo centre at each snapshot. Then, in Section 3.2.2, we analyse the particle trajectories with the velocity and position re-defined with respect to the halo centres.

3.2.1 Tracking of halo centre

CDM haloes typically have asymmetric shape with many substructures, and in a strict sense, the centre of halo is not a well-defined notion. Nevertheless, we may identify the centre-of-mass position near the most significant high-density region as a proxy of the halo centre, and use it to keep track of the bulk motion of a halo. This would provide a robust estimate of the central part of a halo as long as we consider relatively massive haloes.

We start with the haloes identified at $z = 0$ using SO algorithm. We track the identities of the particles near the centre of mass back in time. The exact procedure is summarized as follows:

(i) First, at $z = 0$ data ($n = 99$), pick up the $N_{\rm pickup}$ particles closest to the centre position of halo.

(ii) Go to one snapshot backward ($n = 98$), and use the $N_{\rm pickup}$ particles identified previously to estimate their density-weighted

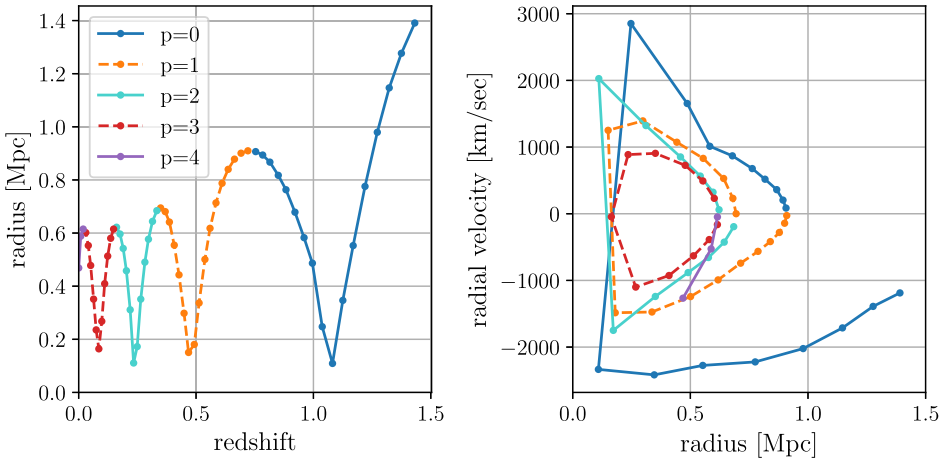

Figure 2. An example of particle trajectory for DM infalling into halo. Points with lines show the time evolution of a DM trajectory stored in the *N*-body snapshots. Left-hand panel plots the radial position as function of redshift, while right-hand panel shows the trajectory in radial phase space. Note that the colours indicate the different number of apocentre passages: $p = 0$ (blue), 1 (orange), 2 (cyan), 3 (red), and 4 (purple).

centre-of-mass position given below

$$\boldsymbol{x}_{\rm halo} = \sum_{i=1}^{N_{\rm pickup}} \frac{\rho_i \boldsymbol{x}_i}{\rho_i}, \tag{8}$$

where $\boldsymbol{x}_i$ is the position of ith dark matter (DM) particle, and ρ_i is the local density at the particle.

(iii) Near the newly estimated centre-of-mass position, pick up again the $N_{\rm pickup}$ closest particles at $n = 98$.

(iv) Go to $n = 97$ data, and use the $N_{\rm pickup}$ particles identified at $n = 98$ to estimate their centre-of-mass position.

(v) Repeat the above steps until we reach the snapshot at $z = 1.43$ ($n = 40$).

In this paper, we choose $N_{\rm pickup} = 128$ particles. The reason why we adopt the density-weighted centre-of-mass position is that rather than a true centre-of-mass position, we wanted to know the densest region of the halo, which would be more stable against the merger event and any disturbances. We have checked that a robust estimation of the halo centre is possible with the density-weighted method above, and the location of the halo centre changes monotonically with time.

After identifying the halo centre at the snapshots $n = 40$–99, the bulk velocity of the halo, $\boldsymbol{v}_{\rm halo}$, is computed using these positions by the second-order finite difference method.

3.2.2 *Identifying particle's apocentre passages*

Having determined the halo centre, we next focus on the trajectories of dark matter particles, and characterize their orbital motion with respect to the halo centre, subtracting its bulk motion. In particular, we wish to clarify the multistream nature of CDM in phase space.

For this purpose, using the multiple snapshots, we identify the apocentre, and count the number of apocentre passages for each particle. To do this, we implement the SPARTA algorithm proposed by Diemer (2017). To be precise, this algorithm is originally used only to identify the splashback radius, i.e. the radius of the first apocentre passage. In this paper, we generalize the algorithm and apply it to identify the subsequent apocentre passages in the inner regions. That is, using the 60 snapshots from $z = 1.43$ to 0, we keep track of each particle trajectory, and measure the radial velocity, $v_{\rm r}$, that is the difference in the peculiar velocities of the DM particle and the halo centre of mass projected along the line of their separation. Namely, at the nth snapshot, this is expressed as

$$v_{{\rm r},n} \equiv (\boldsymbol{v}_n - \boldsymbol{v}_{{\rm halo},n}) \cdot \hat{\boldsymbol{r}}_n, \tag{9}$$

where $\boldsymbol{v}_n$, $\boldsymbol{v}_{{\rm halo},n}$, and $\hat{\boldsymbol{r}}_n$ are the velocity of a DM particle, that of the halo centre, and the unit vector pointing the DM particle from the halo centre, respectively. The sign convention is such that the radial velocity defined above has a negative value for a particle approaching the halo centre. The sign flips to positive when a particle passes the pericentre of the orbit. Conversely, a sign flip from positive to negative happens at the apocentre passage. The location of the first apocentre passage is particularly used to define the splashback radius (Diemer 2017). We further keep tracking the sign flips of radial velocity beyond the first apocentre passage. Counting the number of apocentre passages p for each particle, we classify the particle distribution in phase space by p, which is indeed useful to characterize the multistream structure of haloes.

Fig. 2 shows an example of a particle trajectory extracted from our simulation. Based on the procedure mentioned above, the apocentre passages are identified, and the number of apocentre passages p is incremented after passing through an apocentre (indicated in different colours). As shown in this figure, the procedure works well for isolated haloes with a stationary accretion flow. However, when DM particles are captured by another halo or substructures, they may orbit around the centre of this secondary gravitational source, not the centre of the most prominent haloes of our interest, relative to which the apocentre passages should be examined. In such situations, the sign flip in the radial velocity can also occur due to the internal motion, not at the time of apocentre or pericentre passages. To avoid misidentification of an apocentre passage, we thus monitor the direction of the relative position vector, $\hat{\boldsymbol{r}}_n$, and require an additional condition that the vector must rotate by more than $\pi/2$ between adjacent apocentre passages. We checked that this ensures in most of the cases that the number p is incremented only at the apocentre passage.

Finally, we repeat the procedure for all of the DM particles within $4R_{200}$ at $z = 0$, and create, for each halo, the list of the number of apocentre passages p for the DM particles, which is used to classify the particles in the phase-space distribution. Fig. 3 shows the representative examples. Here, we select four specific haloes,

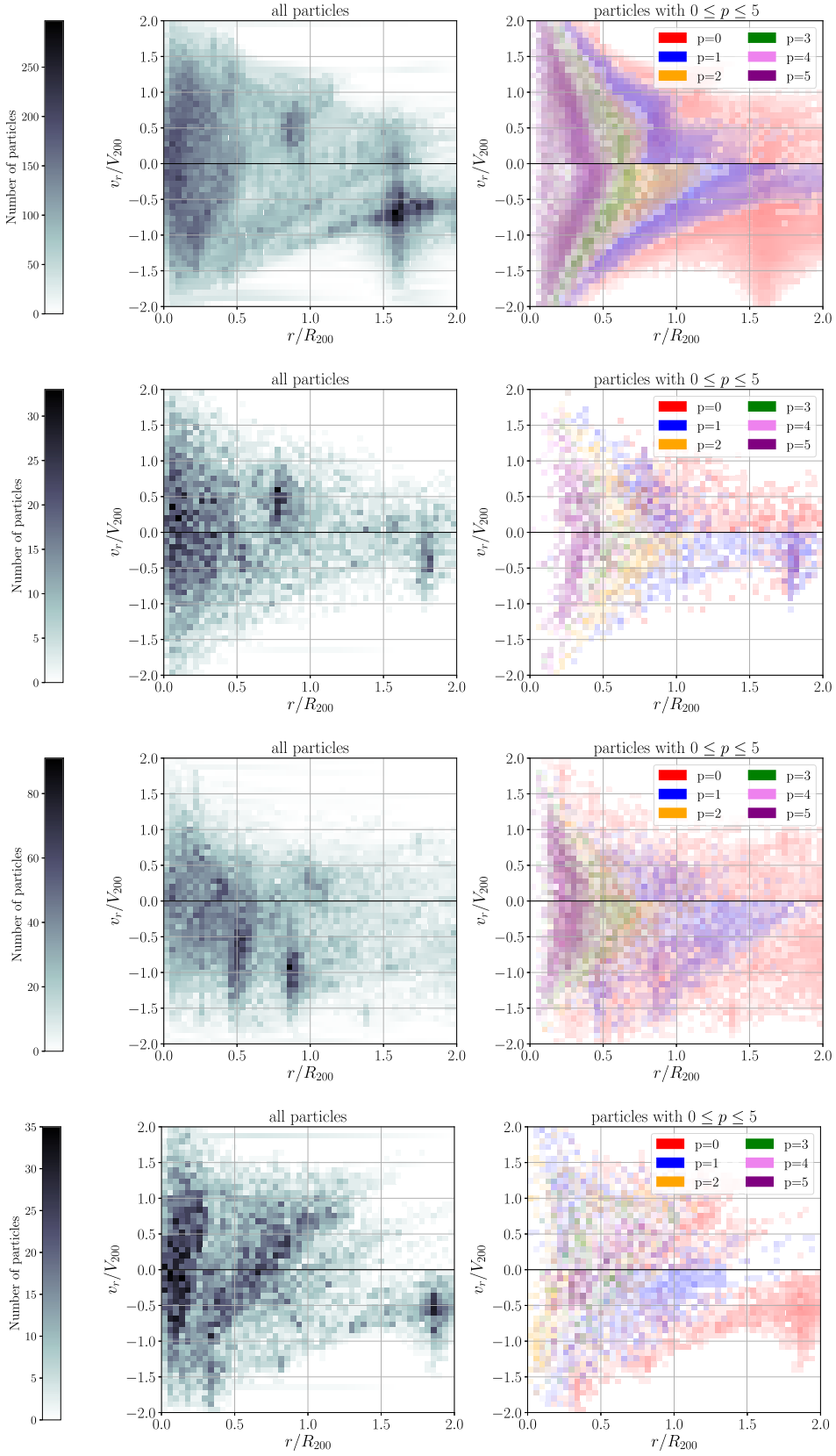

Figure 3. Radial phase-space distribution of DM particles for representative four haloes. Left-hand panels show the phase-space distribution for all DM particles near the selected haloes without classification. Darker colour indicates higher density. Right-hand panels also plot the same phase-space distribution as shown in the left-hand panels, but DM particles are classified with the number of apocentre passages, p, and are plotted in different colours. Note that in right-hand panels, we plot only the particles with $p \leq 5$, and others with $p \geq 6$ are removed.

and plot for each halo the radial phase-space structure. Left-hand panels show all DM particles near the halo, while in right-hand panels, DM particles are classified with the number of apocentre passages, p, and plot them in different colours.

Comparing between left-hand and right-hand panels, we see that the bulk of the phase-space distribution is dominated by the particles with $p = 0$, which are not properly the members of halo. The distribution of these DM particles exhibits irregular and extended structures in the presence of the merging haloes/subhaloes. On the other hand, except the last case (bottom panels), phase-space distributions of the particles with $p \geq 1$ look rather regular shape with a clear segregation of the particles with different p. Apart from the thick width of their distributions, each of the phase-space structures resembles the multistream features predicted by self-similar solution as shown in Fig. 2.

To see more clearly, in Figs 5–8, we separately plot in top panels the radial phase-space distributions tagged with the number of apocentre passages, p. Here, darker colour implies higher density. Also, projected particle distributions in position space are shown in middle panels, while in bottom panels, the cumulative contribution of the density profile from the particles larger than p is shown in different colours. As increasing p, we see clearly that particle distribution tends to get more clustered and rounder, though asymmetric features or substructures are also observed unlike the spherical self-similar solution. These trends motivate us to compare with the self-similar solution in more quantitative way. We will thus discuss in detail how to compare the measured phase-space distributions with self-similar solution in next subsection.

3.3 Fitting the self-similar solution to the phase-space diagram

We here describe the procedure to compare the simulation data with self-similar solution by Fillmore & Goldreich (1984). The self-similar solution provides both the time evolution of each mass element and the resultant snapshot of particle distribution in phase space at a given epoch [see equation (7)]. As shown in Figs 5–8, we are particularly interested in characterizing the multistream nature of DM velocity flow, constructed with particle distributions tagged with the number of apocentre passages, p. Since the particles having the same value of p are supposed to reside at the same stream line, we can conversely use the information on the apocentre passages for each DM particle to detect and identify the stream lines, whose location and shape can be predicted by the self-similar solution for a given set of model parameters. We shall thus fit the self-similar solution to the multiple stream lines for each halo in radial phase space.

To best reproduce the multistream flow from self-similar solution, for each p, we divide the particle distribution in phase space into 14 linearly equal bins in radial velocity, ranging from $-(7/4)V_{200}$ to $(7/4)V_{200}$, where $V_{200} = \sqrt{GM_{200}/R_{200}}$ is the circular velocity at the radius R_{200}. The corresponding bin width is $V_{200}/4$. For each velocity bin labelled by i, we use particles inside the bin to compute the median $r_{p,i}$ and the standard deviation $\sigma_{p,i}$ of the radial position. In top panels of Figs 5–8, the estimated values of $r_{p,i}$ and $\sigma_{p,i}$ are depicted as filled black diamonds with errorbars. Large radial velocity bins tend to have small number of particles, which potentially lead to a biased estimation of median values. To compensate it, we inflate the error bars as

$$E_{p,i}^2 = \sigma_{p,i}^2 \left(1 + \sqrt{\frac{2}{n_{p,i} - 1}}\right), \tag{10}$$

where $n_{p,i}$ is the number of particles in the ith radial velocity bin. Note that the second term at right-hand side of this equation is the 'error of error' due to the Poisson noise. Since the fitting result is generally prone to be strongly affected by bins with small number of particles, the correction given above alleviates this to some extent. To be more conservative, we also ignore bins with $n_{p,i} < 5$, in fitting the data to self-similar solution.

Note that instead of the standard deviation given above, one may adopt the error on the mean in our fitting analyses given below. This would give us much smaller error bars by an extra $1/\sqrt{n_{p,i}}$ scaling, and one can test the spherical self-similar solution in a very strict sense. However, given the non-sphericity and the non-stationary accretion of haloes in simulations, it is easy to expect that the χ^2 values of the fitting using the error on the mean would be much larger than the number of degrees of freedom. We have confirmed this explicitly using some of the haloes in our sample. In the same sense, the non-zero scatter in $r_{p,i}$ also implies that there exists no exact spherical halo with stationary accretion. Since we are rather interested in the bulk properties of each halo taking spherical average, we prefer to use the median of $r_{p,i}$ and the standard deviation at equation (10) as the representative radial distance and spread in the particle distributions, and test the phase-space trajectories of DM particles in a statistical sense.

Having obtained the binned data set in radial velocity space for each p, we compare these data with self-similar solution expressed in the dimensionless coordinates as follows:

$$(r/R_{200}, v_r/V_{200}) = \left(C\Lambda(\tau),\ U\tau^{1-\beta}\frac{\mathrm{d}\lambda}{\mathrm{d}\tau}(\tau)\right), \tag{11}$$

with the function Λ defined by $\Lambda(\tau) = \tau^{-\beta}\lambda(\tau)/\{\tau_{\rm sp}^{-\beta}\lambda(\tau_{\rm sp})\}$. Note that $\tau_{\rm sp}$ corresponds to the epoch of the first apocentre passage. Here, the quantities C and U are the scaling parameters for position and velocity, respectively. Comparison of equation (11) with equation (7) implies $C = R_{\rm sp}/R_{200}$ and $U = \{r_{\rm ta}(t)/t\}/V_{200}$, where t is the age of the universe. In principle, the parameter U can be determined once the values of C, t, β or equivalently s, and R_{200} are fixed. However, the relation between U and other parameters assumes strict self-similarity and spherical symmetry during the entire history of halo evolution in an isolated set-up. In particular, the age of the Universe t in the self-similar solution corresponds to the age of halo counting from its formation time, which is somewhat ambiguous notion. Hence, in our fitting analysis, we do not relate U with other parameters, but rather treat both U and C as independent free parameters.

To sum up, the free model parameters in self-similar solution are C, U, and s. These are determined by the likelihood analysis minimizing the function χ^2

$$\chi^2(C, U, s) = \sum_{p=1}^{p_{\rm max}}\sum_{i=1}^{i_{\rm max}} \frac{1}{E_{p,i}^2}\left[r_{p,i} - R_{200}\,\mathcal{R}_{i,p}(C, U, s)\right]^2, \tag{12}$$

where p and i respectively run over the label of apocentre passages and the radial velocity bins, and we set $p_{\rm max}$ and $i_{\rm max}$ to 5 and 14, respectively. Note that the summation over the radial velocity bins in equation (12) is performed for the bins having more than five particles ($n_{p,i} \geq 5$). Here, $r_{p,i}$ is the median value of the radial positions for particle data at ith radial velocity bin with the number of apocentre passage p. The function $\mathcal{R}_{p,i}$ represents the prediction of self-similar solution, which is the radial position for the stream line corresponding to the number of apocentre passage p at the ith radial velocity bin, given by equation (11). For a given set of parameters, self-similar solution is computed, and the output results

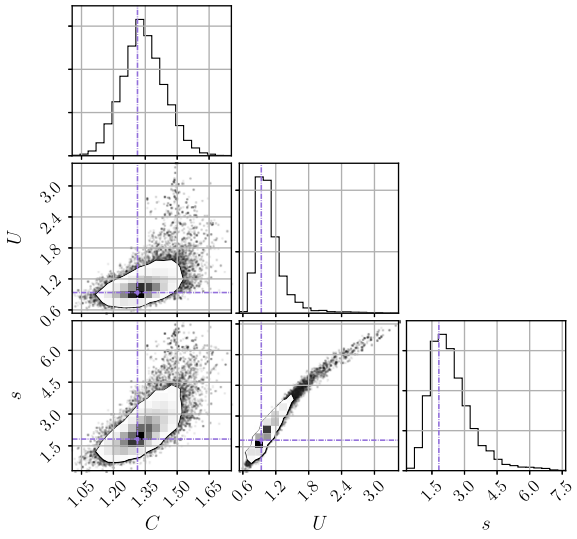

Figure 4. An example of the MCMC parameter estimation for a typical massive halo. The plot summarizes the marginalized two-dimensional posterior distribution for the parameters characterizing the self-similar solution, C, U, and the accretion rate s, discarding the steps in the burn-in period. Note that the parameters C and U are related to R_{200} and V_{200} through $C = R_{200}/R_{\rm sp}$ and $U = r_{\rm ta}/t/V_{200}$, where $R_{\rm sp}$ is the splashback radius, and $r_{\rm ta}$ is the turnaround radius. In each panel, the vertical and horizontal dot–dashed lines indicate the best-fitting values of model parameters. Top panels summarize the one-dimensional projected posterior distribution for each parameter. Visualization of these MCMC results was made with CORNER (Foreman-Mackey 2016).

are tabulated numerically in the form of equation (11) as function of τ. Then, we can identify the stream line that corresponds to the pth apocentre passage, from which we can further read off the radial position r/R_{200} at the ith radial velocity bin. In this way, we obtain $\mathcal{R}_{i,p}$, which is finally plugged into equation (12). For an efficient computation of $\mathcal{R}_{i,p}$, we store the tabulated data set of self-similar solution finely sampled with every 0.1 in parameter space of s, and linearly interpolate these data to obtain a new solution for the target value of s. We confirmed that the linearly interpolated results are converged to those obtained by quadratic interpolation and no significant difference is found.

Based on equation (12), we use the Markov chain Monte Carlo (MCMC) algorithm to explore the model parameters for each haloes, imposing the following uniform priors:

$$C \in [0, 5], \quad U \in [0, 5], \quad s \in [0, 9]. \tag{13}$$

These parameter ranges are large enough that they do not affect the best-fitting values and tails of the posterior distributions. Making use of the public python code, EMCEE (Foreman-Mackey et al. 2013), we calculated 4000 steps with 12 walkers for all the 11 296 haloes. The length of the chain would be sufficient to obtain convergent posterior distributions: the autocorrelation time of the MCMC chain is less than 1000 steps (typically a few hundred steps with slight variation among different haloes).

For illustration, we show in Fig. 4 the results of MCMC analysis for a cluster-sized halo. The plotted results are the marginalized two-dimensional posterior distribution for the model parameters, discarding the first 800 steps for each walkers as the burn-in period. As shown in Fig. 4, there is a unique maximum in density which is very close to the best-fitting values of model parameters, depicted as the crossing point of the dot–dashed lines. We checked that the example shown here is typical, and the best-fitting value is close to the peak position of posterior distribution.

4 RESULTS

This section presents the main results of this paper, and gives a detailed comparison of the multistream flow of DM particles in the N-body simulation with the prediction of the self-similar solution from the phase-space point of view. Section 4.1 presents the MCMC analysis based on Section 3.3. Section 4.2 presents the properties of the MCMC results for all of the haloes identified at $z = 0$, and discusses the selection of halo samples better fitted to the self-similar solution. Then, Section 4.3 shows the statistical properties of the model parameters for the well-fitted haloes.

4.1 Comparison of representative haloes with self-similar solution

Here, for illustrated purpose, we pick up four representative haloes among the total of 11 296, and in the upper panels of Figs 5–8, the binned phase-space distribution of the DM particles labelled by the number of apocentre passage p (black filled circles with errorbars) is compared with the best-fitting self-similar solution, depicted as the yellow solid lines. Also, as we have seen in Section 3.2.2, the middle and bottom left panels of Figs 5–8 present the particle distributions for each p on a two-dimensional projected position space, while the bottom right panels plot the density profiles for the cumulative contributions of the particles experienced at least p apocentre passages.

The first and second example of the haloes, shown in Figs 5 and 6, are the phase-space structure well fitted by the self-similar solution, with the best-fitting values of s being $s = 1.81$ and 2.81, respectively. The mass of these haloes are $M_{200} = 1.23 \times 10^{15}$ and $1.16 \times 10^{14}\,{\rm M}_\odot$, respectively. As it is clear from the figures, the predictions with the best-fitting parameters reproduce the measured phase-space distribution binned along the velocity axis remarkably well. The particle distributions of these haloes in position space, seen in the bottom left panels of Figs 5 and 6, exhibit substructures or clumps, and their global shape is indeed asymmetric. Nevertheless, as increasing p, the particle distributions gets smoother, and tend to be rounder. Further, the best-fitting values of s indicate that the asymptotic slope of the density profile is -2, i.e. $\rho \propto r^{-2}$ [see equation (3)], which in fact agrees well with inner slope of the measured density profile, shown in the bottom right panels of Figs 5 and 6.

The third example, shown in Fig. 7, is a halo with mass $3.07 \times 10^{14}\,{\rm M}_\odot$, three times larger than the second example. Although the best-fitting self-similar solution seems to explain the overall trends of the binned phase-space distribution from the simulation well, a closer look at the simulation data at $p = 1$ reveals a structure elongated vertically at $v_{\rm r}/V_{200} < -1$, and a systematic discrepancy between the simulation and the model is manifest around this structure. This corresponds in position space to a large blob at $(x, y) \simeq (0.5\,R_{200}, 0)$ shown in the leftmost panel in the middle row. The discrepancy is mostly ascribed to this component with significant scatter in the radial velocity, just experienced the first apocentre passage after a major merger. Also, in the position plot for the particles with $p = 0$ (second from the left in the bottom row), we can observe several significant substructures near the centre. These are before the merger to the main halo as indicated by the fact that they have $p = 0$. The existence of these features might also have disturbed the orbits of the already accreted DM particles. Since the

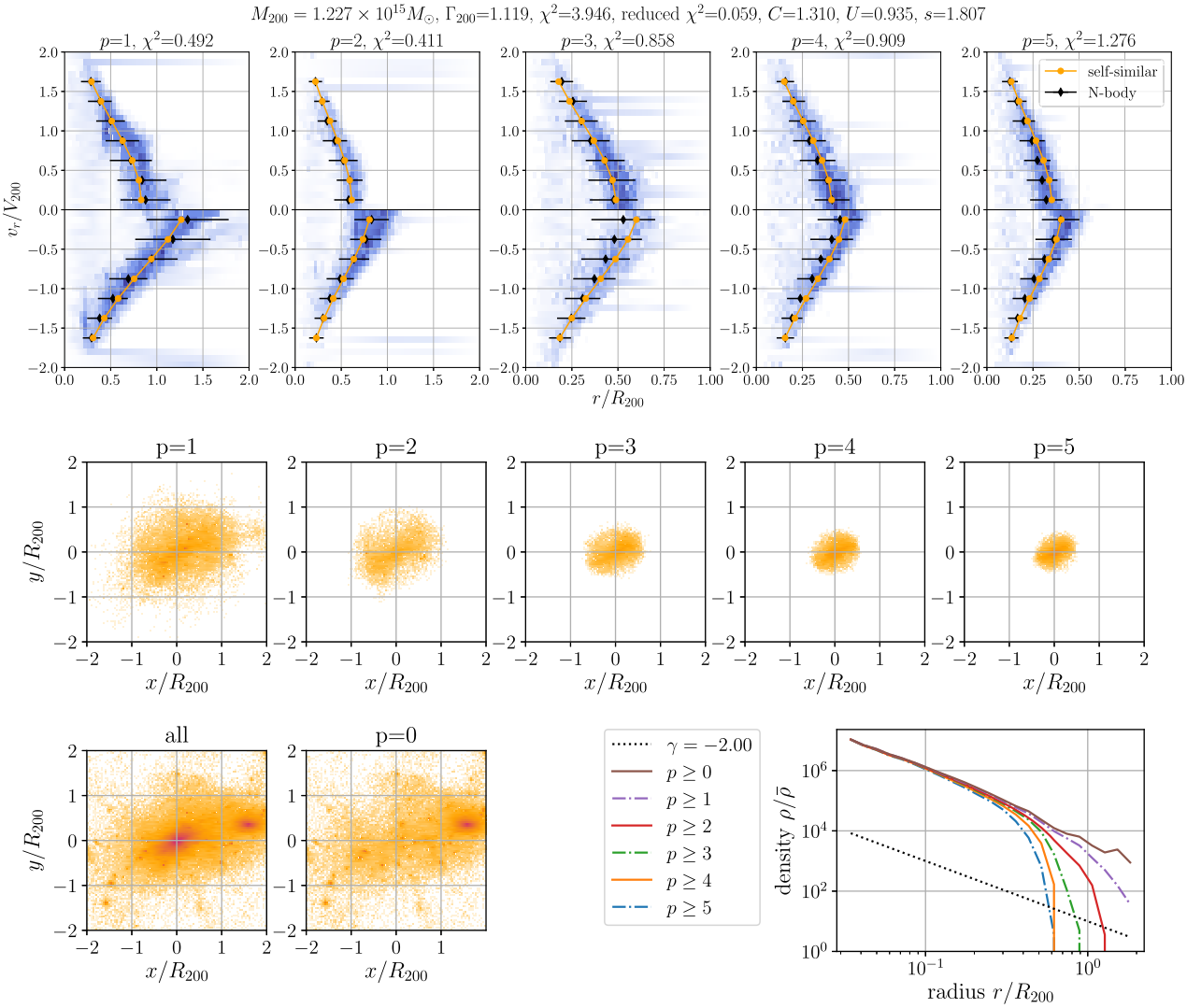

Figure 5. A cluster-sized halo with $M_{200} = 1.227 \times 10^{15}$ M$_\odot$, which apparently shows a good agreement with self-similar solution (see Section 4.2). This is the same halo as shown in the top panels of Fig. 3. *Top*: radial phase-space distribution of N-body particles with $p = 1, 2, \cdots, 5$ (denoted by blue colour contrast) with the best-fitting self-similar solution (denoted by orange lines). Particles with different number of apocentre passages, p, are shown in different panels. Filled diamonds indicate the medians of N-body distributions in each velocity bin with error bars defined at equation (10). *Middle and bottom*: projected distribution of DM particles in position space (middle five panels and bottom two panels) and cumulative contribution to the radial density profile (bottom right panel), classified with number of apocentre passages, p.

self-similar solution by Fillmore & Goldreich (1984) describes an isolated halo with stationary accreting matter, this is, in a sense, a typical example violating the basic assumption of the model.

On the other hand, the fourth example, shown in Fig. 8, has a mass similar to the second example with a much smaller value of the best-fitting parameter, $s \simeq 0$. Visually, the agreement between the self-similar solution and the simulation is bad. In contrast to the third example, a large discrepancy is now found in the phase-space distribution at $p > 3$. Because of this, the inner slope of the measured density profile does not agree well with that of the best-fitting self-similar solution (see the bottom right panel). Looking at the particle distribution in position space at $z = 0$, we find that unlike the previous examples, the spatial extent of the particle distribution does not shrink with increasing p for $p \geq 3$. Although, we do not see any clear signature of the clumps or substructures at $p \geq 1$, we suspect that the discrepancy is due to the remnant of orbiting substructures which is tidally stripped. In fact, going back to the snapshots at slightly earlier time, we confirm that this halo underwent a major merger with a small impact parameter, and the infalling halo exhibited a rapid orbital decay followed by the tidal stripping. Thus, the example shown here may not be regarded as a relaxed halo, though it is difficult to judge only from the spatial distribution at the final snapshot. In this respect, the phase-space distribution is more informative, and is powerful to probe the dynamical properties of halo structure.

In Figs 5–8, we also show the values of both χ^2 and the reduced χ^2 for the best-fitting model. Note that the number of degree of freedom to derive the reduced χ^2 varies by haloes because of the different number of available velocity bins, but it typically ranges from 50 to 70. In agreement with visual inspection of the radial phase-space plots, the first example has the smallest χ^2 among the four representative examples, and the fourth example has the largest χ^2 value. However, their reduced χ^2 values are rather small, and both are less than 1. These small values basically come from the

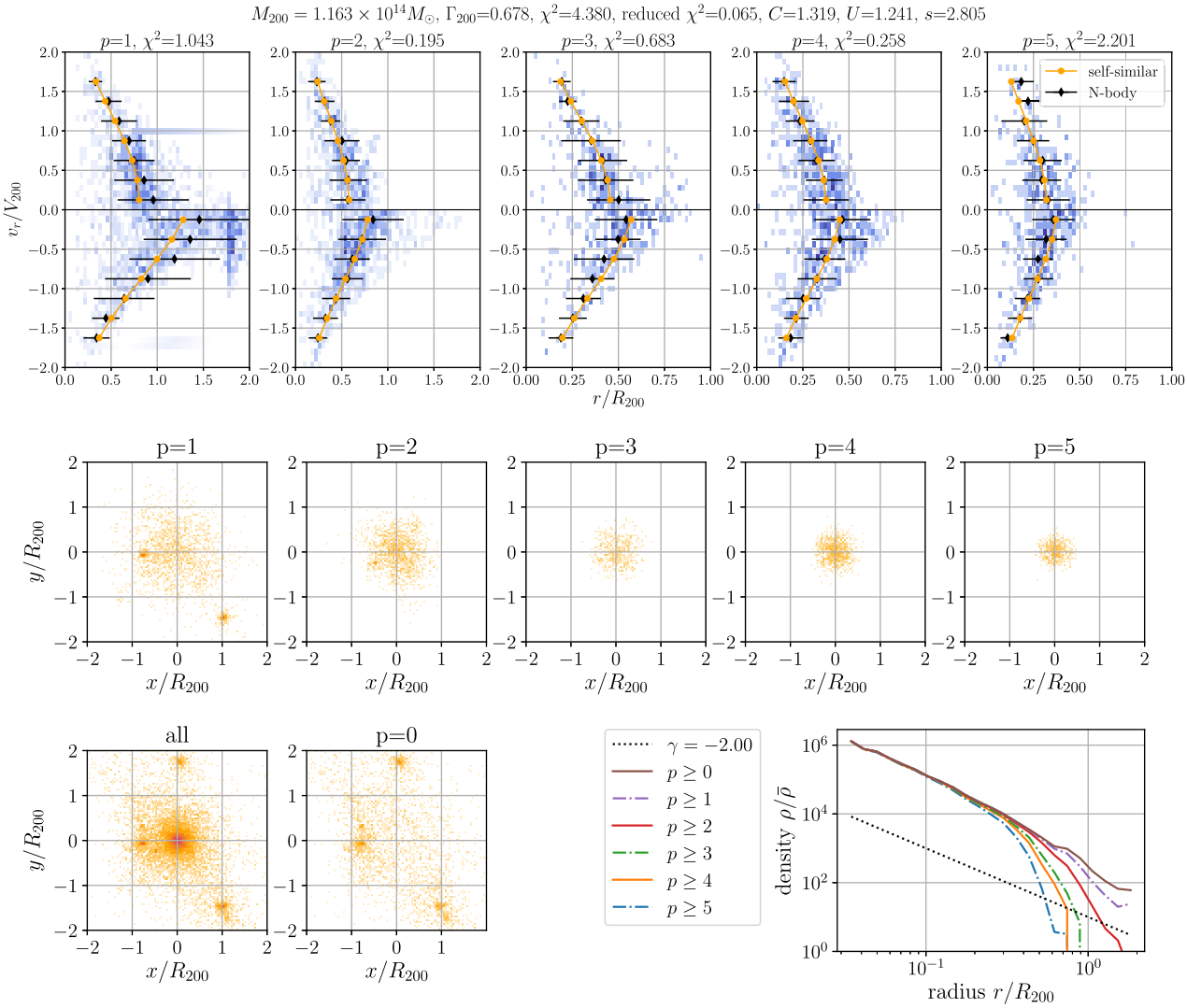

Figure 6. Same as in Fig. 5, but for a slightly less massive halo with $M_{200} = 1.163 \times 10^{14}\,\mathrm{M}_\odot$. This is the same halo as shown in the second from the top in Fig. 3.

rather loose error we adopted in estimating χ^2 [see equation (10) and the subsequent paragraph on our choice of the error bars]. Thus, in order to study the properties of haloes 'well fitted' by the self-similar solution in our sense, the χ^2 values or the reduced χ^2 values alone are insufficient. We have to come up with other additional requirements or criteria to form a sample of well-fitted haloes.

4.2 Sample selection

Applying the method described in Section 3, we have analysed 11 296 haloes whose virial masses M_{200} are greater than $10^{13}\,\mathrm{M}_\odot$. As we have seen in Section 4.1, the self-similar solution sometimes fails to describe the multistream structure of phase-space distribution for haloes in *N*-body simulation. A part of the reason is ascribed to the fact that some haloes near the low-mass end do not have sufficient number of particles to determine the location of the streams to be compared in detail with the self-similar solutions. In order to quantitatively clarify the extent to which the self-similar solution can describe the multistream feature of haloes in radial phase space, one may introduce strict selection criteria for each halo well fitted by the self-similar solution. Although this leaves us only a biased subset of simulated haloes, their statistics would give us useful insight on the structure of more realistic haloes.

First condition we impose is that the number of radial velocity bins having DM particles more than five should be at least 48 out of 70 over $p = 1$–5 [condition (i)]. This excludes 2924 haloes, leaving 8372. Next, we exclude the haloes for which the radial position of the stream line is not well determined like those shown in Fig. 8 ($p = 3$–5). This can be originated from different reasons: a significant fraction of particles failed to be assigned the correct number of apocentre passages due to the limitation of our algorithm, or the actual phase-space distribution is far from self-similar solutions due to the major merger, a large number of substructures, or highly asymmetric shape. The χ^2 defined at equation (12) alone cannot perfectly isolate these haloes as 'badly fitted' because a poor determination of the particle trajectories generally leads to a large value of $E_{p,i}$ [see equation (10)]. We thus impose another condition to exclude those haloes from the later analyses as follows. For each stream line and at each radial velocity bin, we compute the ratio, $E_{p,i}/\bar{r}_{p,i}$, where $\bar{r}_{p,i}$ is the median value of radial position for particles in the ith velocity bin for particles after the pth apocentre passage. This ratio indicates how well we can determine the median

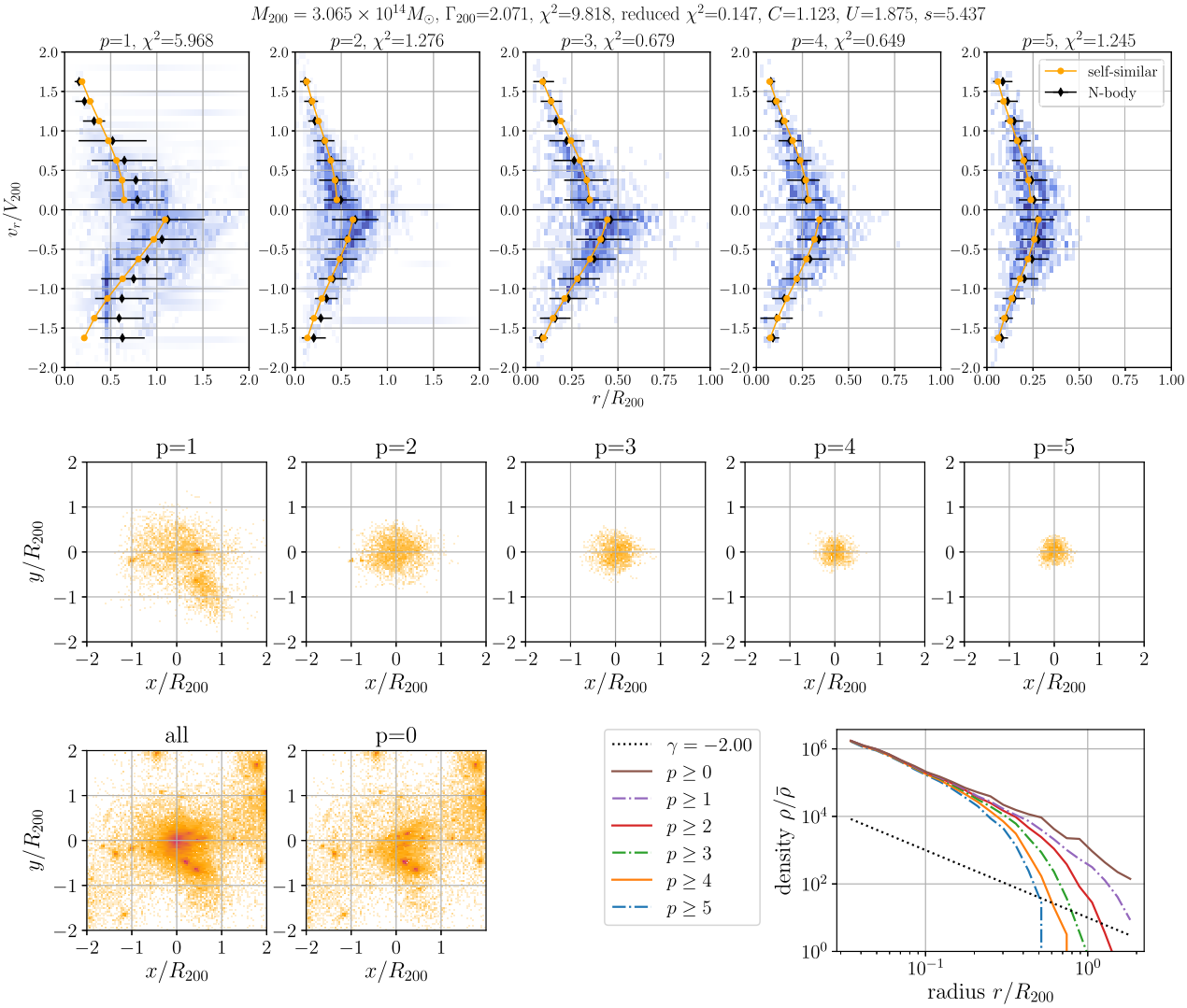

Figure 7. Same as in Fig. 5, but for a halo excluded by the condition (iii) given by equation (14) (See Section 4.2). Note that this is the same halo as shown in the second from the bottom in Fig. 3.

location of the stream line. We then exclude the halo in which the seventh largest value of this ratio is greater than 0.625 [condition (ii)]. With this condition, 4108 haloes are excluded.

Applying the conditions mentioned above, we now assess the *goodness of fit* using the minimum value of χ^2 obtained from the MCMC analysis. We impose [condition (iii)]

$$[\chi^2]_p \leq 3.5, \quad (p = 1, \cdots, 5), \tag{14}$$

where the subscript p indicates that χ^2 is computed only for the particles with p apocentre passages. The halo shown in Fig. 7 is a typical example excluded by this third condition, and a significant deviation from the self-similar solution is found for the first apocentre passage $p = 1$, $\chi^2_{p=1} = 5.968$. Note that with this last condition, haloes whose phase-space particle distribution apparently resembles the best-fitting self-similar solution are sometimes excluded. In this respect, the resultant samples that meet all the selection criteria may be regarded as conservative and high-quality haloes well described by self-similar solution. We label these haloes as 'well-fitted' samples.

Table 2 summarizes the number of haloes that meet each of the selection criteria. To see how our criteria gives (un-)biased halo samples, we plot in Fig. 9 the frequency distribution of haloes against the quantities characterizing the individual halo properties. The left-hand panel shows the distribution against the reduced χ^2. We see that the condition (i) preferentially removes haloes having a rather large value of reduced χ^2. Combining the condition (ii) further excludes haloes mainly with large reduced χ^2, but there still remain haloes with a moderately large reduced χ^2 survived. Adding the third condition, those haloes are finally removed, and the resultant frequency distribution exhibits a sharp cut-off around the reduced $\chi^2 \sim 0.3$, which is consistent with equation (14) for the individual orbit specified by p given that the total degree of freedom over $1 \leq p \leq 5$ in the likelihood analysis is roughly around 50–70.

The middle panel of Fig. 9 shows the frequency distribution against the mass accretion rate, Γ_{200}, directly measured from the N-body simulation, which is defined as follows (e.g. Diemer & Kravtsov 2014):

$$\Gamma_{200} := \frac{\Delta \ln M_{200}}{\Delta \ln a}, \quad \Delta X \equiv X(z = 0) - X(z = 0.5). \tag{15}$$

The definition above has been used in the literature as an indicator to characterize the environmental dependence of the splashback

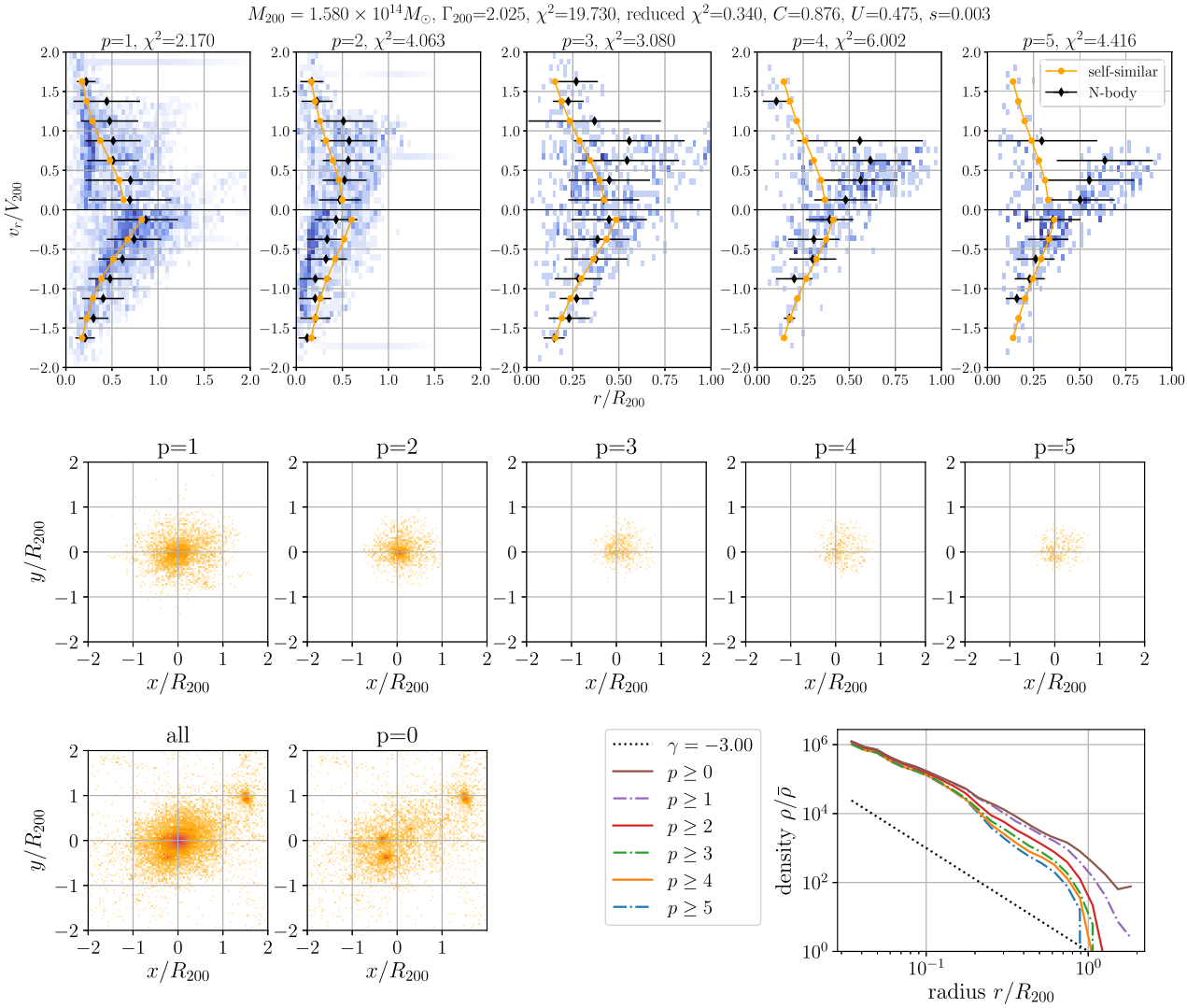

Figure 8. Same as in Fig. 5, but for a halo excluded by the condition (ii). This is the same halo as shown in the bottom panel of Fig. 3.

Table 2. The number of haloes meeting our selection conditions.

Conditions	Number of haloes
None	11 296 (100 per cent)
(i) Sufficient particles in most of the bins	8372 (74.1 per cent)
(i) + (ii) Good orbit determination	4264 (37.0 per cent)
(i) + (ii) + (iii) Well fitted by the self-similar solution	3561 (31.5 per cent)

radii on top of the rather trivial mass dependence. A notable feature seen in the frequency distribution is that the condition (ii), which rejects haloes with large uncertainties in the locations of stream shells, almost determines the accessible range of Γ_{200} for the final samples, excluding the haloes having a large value of Γ_{200}. This implies that a rapid mass accretion tends to disturb the trajectories of DM particles inside the halo, thus leading to a wider stream line/shell, i.e. the radial distribution of particles having the same value of p for a given radial velocity.

Finally, the right-hand panel of Fig. 9 shows the frequency distribution against the halo mass M_{200}. While the condition (i) removes light haloes almost only in the range $M_{200} \lesssim 2 \times 10^{13}\,\mathrm{M}_\odot$, the other two conditions do not change the shape of the distribution. As a result, the final sample of haloes can be regarded as a representative sample of the original in terms of mass, except for the lightest end. This is in marked contrast to the effect of the selection on the accretion rate.

To conclude, one should keep in mind that our final sample is biased towards low accretion rate, but nearly representative in terms of the halo mass in later analyses. Once these are in mind, a large number of haloes that meet all conditions would allow us to study statistical properties of the multistream nature of CDM haloes.

4.3 Statistical properties of well-fitted halo samples

The halo sample selected in Section 4.2 is characterized not only by the measured values of the mass M_{200} and accretion rate Γ_{200} from usual SO halo definition, but also by the best-fitting parameters in the self-similar solution, i.e. the accretion rate parameter $s_{\rm best}$, and the two dimensionless quantities $C_{\rm best}$ and $U_{\rm best}$. Note that $C_{\rm best}$ represents the ratio of the splashback radius to the radius R_{200}, i.e. $R_{\rm sp}/R_{200}$. As shown in Fig. 4, the parameter $U_{\rm best}$ is strongly correlated with $s_{\rm best}$. Hence, focusing on four other physical parameters, M_{200}, Γ_{200}, $s_{\rm best}$, and $C_{\rm best}$, and also the reduced χ^2 of

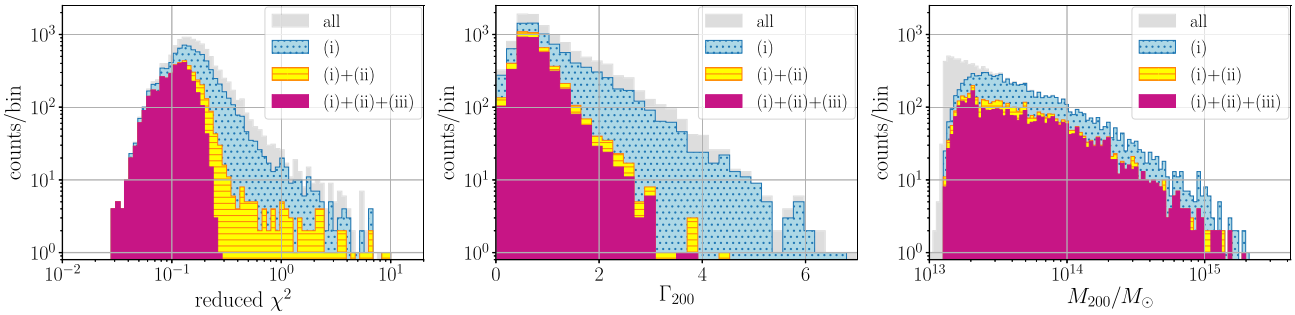

Figure 9. Frequency distributions of haloes against reduced χ^2 (left), accretion rate Γ_{200} (middle), halo mass M_{200} (right) for haloes that meet our selection criteria (see Table 2). Vertical axis represents the number of haloes per bin.

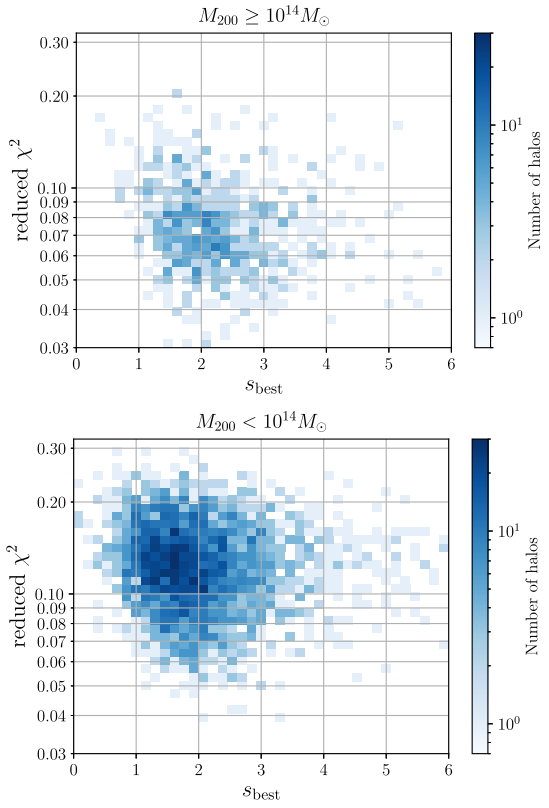

Figure 10. Frequency distribution of haloes plotted in two-dimensional plane of the reduced χ^2 and best-fitting parameter of s, $s_{\rm best}$. Top and bottom panels show the results for well-fitted halo samples with mass greater and less than $10^{14}\,{\rm M}_\odot$, respectively. Colour depth in each pixel indicates the number of haloes falling into the pixel in logarithmic scales.

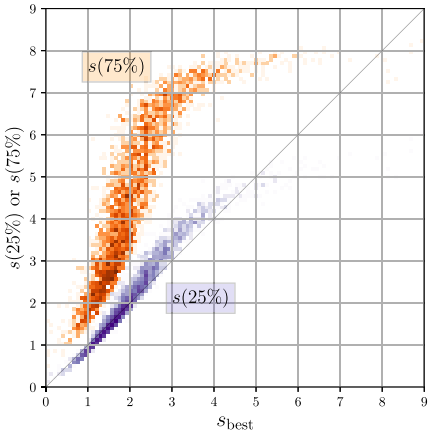

Figure 11. 25 per cent and 75 per cent quantiles of MCMC s-distributions for well-fitted haloes. Horizontal axis denotes the best-fitting s-values. The solid line is plotted for reference, indicating the linear relation, $s_{\rm best} = s(25\text{ per cent})$ or $s(75\text{ per cent})$. Due to the positively skewed posterior distribution, the $s(25\text{ per cent})$ is larger than $s_{\rm best}$ for most of the haloes.

the best-fitting model, we examine the statistical properties of the selected haloes.

First look at the distribution of the parameter $s_{\rm best}$. Fig. 10 shows the distribution of the haloes in our sample after the selection projected on the $s_{\rm best}$–reduced χ^2 plane. We here divide the samples into two subsamples with the halo mass larger than (upper) and less than (lower) $10^{14}\,{\rm M}_\odot$. Fig. 10 shows a clear trend that the massive haloes tend to have smaller reduced χ^2. That is, the multistream structure in the massive haloes is better described by the self-similar solution. A part of the reason may be that massive haloes are not so severely affected by the outer environment, where merger event and asymmetric matter accretion occur. A closer look at the distribution of $s_{\rm best}$ suggests that a larger value of $s_{\rm best}$ is generally favoured for massive haloes. Looking at the uncertainty in the parameter estimation, however, this is not statistically significant.

In Fig. 11, the 25 per cent and 75 per cent quantiles of the posterior distribution of s are evaluated in each halo from the MCMC analysis, and the results are plotted as function of the best-fitting value, $s_{\rm best}$. As we have seen in Fig. 4, the posterior distribution of s is largely skewed with a long tail. This trend is generally seen in most of the haloes in the selected sample, and the size of the 1σ error, Δs, is almost the same as $s_{\rm best}$, i.e. $\Delta s/s_{\rm best} \sim 1$. Note that as increasing $s_{\rm best}$, the distribution of 75 per cent quantile apparently converges to 7–8. This might be partly ascribed to our set-up of the prior $s \in [0, 9]$, but the number of haloes having $s(76\text{ per cent}) \sim 8$ is actually small, and it does not affect the best-fitting values of s at least for the selected halo samples. In any case, with a large scatter in the posterior distribution, the only thing that one can clearly say from the distribution of $s_{\rm best}$ is that the accretion rate parameter lies at $1 \lesssim s \lesssim 3$ for the selected halo samples, and there is no statistically significant difference between massive and less massive haloes.

Next look at the statistical correlation between the measured halo properties and the best-fitting parameters in self-similar solution. Fig. 12 shows the distribution in the plane of $C_{\rm best}$ and Γ_{200} (top) and $C_{\rm best}$ and $s_{\rm best}$ (bottom). Since Γ_{200} and $s_{\rm best}$ are expected to characterize roughly the same thing, i.e. the accretion rate, a naive expectation is that these two panels exhibit a similar trend. However, the resultant correlation properties are rather different.

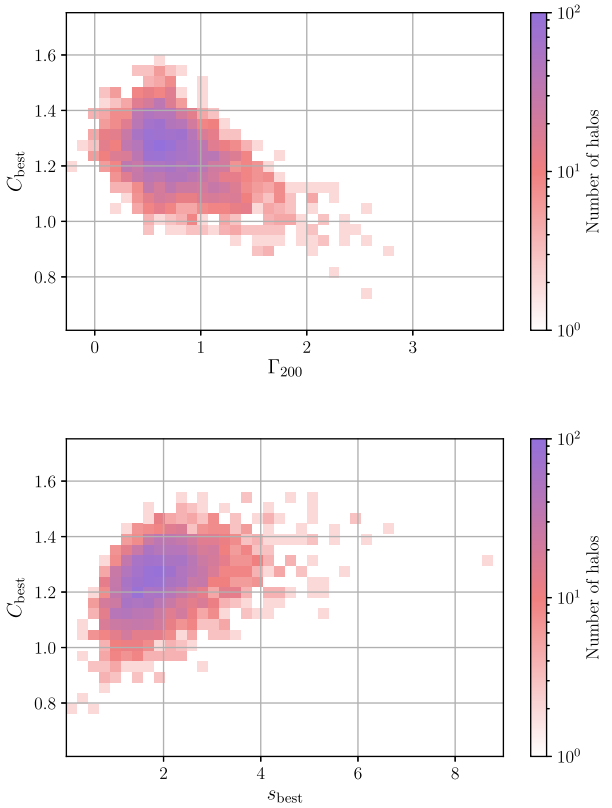

Figure 12. Correlation among the best-fitting parameters in self-similar solution and measured quantity. Top panel shows the correlation between the best-fitting parameter of C (i.e. $C_{\rm best}$) and the measured accretion rate Γ_{200}, while bottom panels present the result between best-fitting values $C_{\rm best}$ and $s_{\rm best}$. Colour depth in each pixel indicates the number of haloes falling into the pixel.

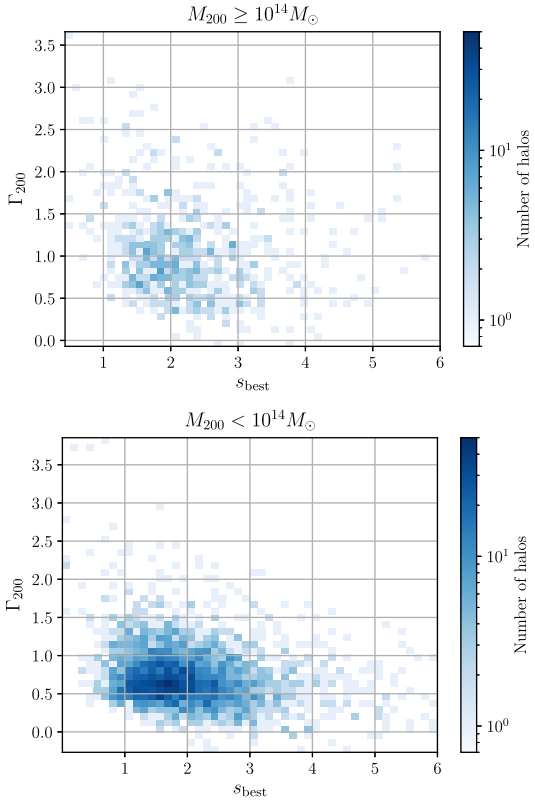

Figure 13. Correlation between the best-fitting value of s and measured accretion rate Γ_{200} for well-fitted halo samples. Top and bottom panels, respectively, show the results for haloes greater and less than mass $M_{200} = 10^{14}\,{\rm M}_\odot$. Colour depth indicates the number of haloes in each pixel.

While the measured accretion rate Γ_{200} exhibits an anticorrelation with $C_{\rm best}$, the best-fitting accretion rate $s_{\rm best}$ looks a weak but positive correlation. Recalling the fact that $C_{\rm best}$ corresponds to $R_{\rm sp}/R_{200}$, the former trend is pretty much consistent with those found in the literature (e.g. More et al. 2015; Diemer et al. 2017).

On the other hand, the weakly positive correlation between $C_{\rm best}$ and $s_{\rm best}$ looks bit puzzling, and seems to contradict with theoretical prediction by Shi (2016), who has derived the analytical relation between the accretion rate and splashback radius based on the self-similar solution. A large difference between Shi (2016) and our analysis is that we treat these parameters free to be determined by fitting the measured phase-space structures to the self-similar solutions. As we discussed in Section 3.3, the parameters C and s are tightly related with each other in an idealistic situation, and Shi (2016) actually used this to derive the correlation property in an analytical way. Thus, the results shown in Fig. 12 suggest a departure from the idealistic situation in the simulated halo samples. In this respect, the fitted values of the accretion rate parameter, $s_{\rm best}$, may not necessarily correspond to the net accretion rate measured at r_{200}, Γ_{200}.

To see it more explicitly, we plot in Fig. 13 the statistical correlation between $s_{\rm best}$ and Γ_{200}. Here, dividing the selected halo samples into two subsamples with mass larger than (upper) and less than (lower) $10^{14}\,{\rm M}_\odot$, the frequency distributions of haloes are shown in the two-dimensional plane. As anticipated, there is little correlation between $s_{\rm best}$ and Γ_{200}, and the trend is almost similar between light and heavy subsamples, although the scatter is relatively large for massive haloes. The result indicates that the two parameters are probing different aspects of the halo accretion history.

5 DISCUSSION

In this section, to better understand the results shown in Figs 12 and 13, we investigate the physical meaning of the parameter $s_{\rm best}$, and look for a link to other quantities measured from N-body simulations. For this purpose, we decompose the mass of each halo into different contributions, each of which consists of DM particles with different numbers of apocentre passages. Then, we consider the contribution coming from the DM particles having $p \geq p_{\rm min}$ at redshift z. Denoting the mass of such a contribution by $M_{p\geq p_{\rm min}}(z)$, we define the new accretion rate parameters, which should be more relevant to the multistream flows inside the splashback radius as

$$\Gamma_{p\geq p_{\rm min}} = \frac{\Delta \ln M_{p\geq p_{\rm min}}}{\Delta \ln a}. \tag{16}$$

In evaluating equation (16), the finite difference, $\Delta \ln M_{p\geq p_{\rm min}}$, is taken between $z = 0$ and $z = 0.11$, not $z = 0$ and $z = 0.5$, which we adopted in measuring Γ_{200} [see equation (15)]. The reason is that increasing z as well as p, a reliable estimation of the number of apocentre passages becomes difficult due to the limited range of available redshifts ($z \leq 1.43$ in our case). The closer redshift interval used in equation (16) gives us a more instantaneous estimate of the mass accretion.

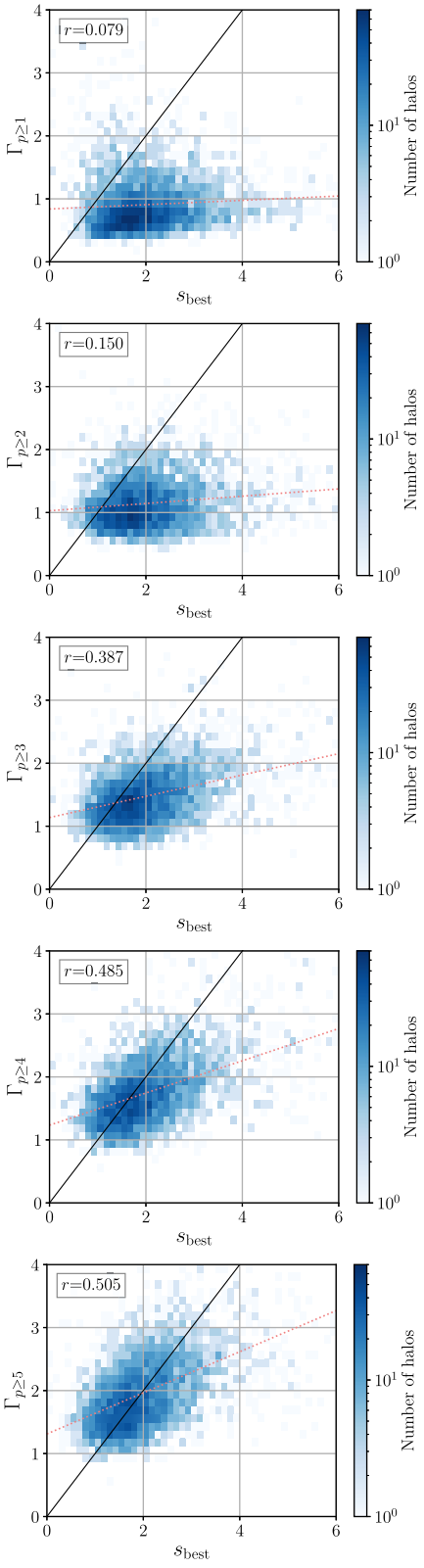

Figure 14. Correlation between $s_{\rm best}$ and $\Gamma_{p\geq p_{\rm min}}$ defined at equation (16) for well-fitted halo samples. From top to bottom, the results with $p_{\rm min} = 1$–5 are respectively shown. Colour depth in each pixel indicates the number of haloes in logarithmic scales. Dotted lines are the linear regression estimated by least-squares method, and the derived values of Pearson's correlation coefficient, denoted by r, are also shown in each panel. For reference, linear relations of $s_{\rm best} = \Gamma_{p\geq p_{\rm min}}$ are also plotted in black solid lines.

Fig. 14 shows the correlations between $s_{\rm best}$ and $\Gamma_{p\geq p_{\rm min}}$ for $p_{\rm min} =$ 1–5 (from top to bottom). In each case, we perform linear regression and plot the result by the red dotted line. Also, we estimate the Pearson correlation coefficient r, and the derived values are shown in each panel. For reference, the linear relation of $s_{\rm best} = \Gamma_{p\geq p_{\rm min}}$ is also plotted in black solid line. As increasing $p_{\rm min}$, the estimated values of $\Gamma_{p\geq p_{\rm min}}$ get large and exceed the mean value of Γ_{200} (roughly $\sim$1). This is presumably because we are preferentially looking at the inner halo structures, where the inward streaming flows become dominant. By contrast, the inward accretion flow near the halo boundary is prone to be disturbed by the outer environment, and hence $\Gamma_{p\geq p_{\rm min}}$ tends to get larger than Γ_{200}. A notably interesting trend we find is that the correlation between $s_{\rm best}$ and $\Gamma_{p\geq p_{\rm min}}$ gets tighter as increasing the minimum number of apocentre passages, $p_{\rm min}$. The trend is, indeed, more clearly seen in the Pearson correlation coefficient, and quantitatively, the coefficient increases from 0.079 to 0.505 as we change $p_{\rm min}$ from 1 to 5. Further, the slope of the linear regression gets inclined, approaching to $s_{\rm best} = \Gamma_{p\geq p_{\rm min}}$, though the regression coefficient is still 0.67 at $p_{\rm min} = 5$. The result suggests that the parameter $s_{\rm best}$ is determined by the inner multistream flows with a large value of p. In other words, the best-fitting value of s carries some information on the memories of the early-phase mass accretion history. By contrast, the accretion rate Γ_{200} is sensitive to the recently accreting matter near the halo boundary. In this sense, little correlation between $s_{\rm best}$ and Γ_{200}, shown in Fig. 13, may be regarded as a reasonable outcome.

Finally, it would be interesting if the quantity similar to $s_{\rm best}$ can be measured directly from observations. The complementarity of the parameter s to Γ_{200} gives a fruitful insight into the history of the halo formation and evolution over a longer period of time. Due to the fact that we can measure only the line-of-sight component of the velocity and/or confusion between Hubble flow and peculiar velocity, it is not actually straightforward to get access to the phase-space structure (but see e.g. Biviano et al. 2013; Munari, Biviano & Mamon 2014; Abdullah, Wilson & Klypin 2018). Nevertheless, as we have seen in Section 2, the parameter s is related to the inner slope of a halo [equation (3)]. Although it is indirect, the density slope could provide a useful hint to infer or pin down the early-phase mass accretion history of a halo. Other proxies, such as the colour or morphological information for galaxies, might be useful to infer the streams in the phase space.

6 CONCLUSIONS

In this paper, we have studied the radial phase-space properties of CDM haloes in a cosmological N-body simulation. In particular, we have quantified the multistream structures of haloes inside the splashback radius, and their radial phase-space distributions are compared with the spherically symmetric self-similar solution by Fillmore & Goldreich (1984). In order to trace and characterize the multistream nature of each halo in N-body simulation, we implemented the SPARTA algorithm developed by Diemer (2017) to keep track of the trajectories of dark matter particles. We extended it to identify the inner apocentre passages inside the so-called splashback radius, and count its number along each trajectory of dark matter particle. With the particle distribution characterized by the number of apocentre passages, the multistream nature of dark matter velocity flows can be visualized in phase space, and we were able to make a detailed comparison of the phase-space properties with the predictions of the self-similar solution. Using MCMC technique, we have analysed in total 11 296 haloes with

mass $M_{200} \geq 10^{13}\,\mathrm{M}_{\odot}$ to obtain the best-fitting parameters of the self-similar solution characterizing the multistream flows inside the haloes in *N*-body simulation.

Our important findings are summarized as follows:

(i) About 30 per cent of the haloes among those we analysed are classified as well described by the self-similar solution (Fillmore & Goldreich 1984). These haloes are selected by imposing the three conditions discussed in Section 4.2, i.e. (i) sufficient number of particles in most of the radial velocity bins, (ii) a clear determination of stream line/shell tagged with the number of apocentre passages, (iii) a condition for the goodness of fit for each stream given by equation (14) (see also Table 2). Typical examples of well-fitted haloes are shown in Figs 5 and 6. We found that more massive haloes tend to be better described by the self-similar solution with a smaller value of the reduced χ^2 (see Fig. 10).

(ii) The self-similar solution by Fillmore & Goldreich (1984) is characterized by the three parameters: stationary accretion rate s, and scaling parameters in radial position and velocity, C and U, where the parameters C is related to the ratio of splashback to virial radius through $C = R_{\rm sp}/R_{200}$. Allowing these parameters to be free, we determined their best-fitting values in each halo, and found that for the well-fitted halo sample, the best-fitting values of s and C are distributed around the ranges $1 \lesssim s_{\rm best} \lesssim 3$ and $0.9 \lesssim C_{\rm best} \lesssim 1.5$ (see Fig. 12).

(iii) Statistical analysis of the well-fitted halo sample reveals that the best-fitting model parameter $C_{\rm best}$ shows an anticorrelation with the measured accretion rate at R_{200}, Γ_{200} [see equation (15)]. While this is fully consistent with those previously found in the literature, the parameter $C_{\rm best}$ exhibits a weak but positive correlation with the best-fitting accretion rate parameter, $s_{\rm best}$, which apparently contradicts with previous findings. In particular, we found that there is no clear correlation between $s_{\rm best}$ and Γ_{200}. A detailed study on the mass accretion rate (Section 5) indicates that the best-fitting parameter $s_{\rm best}$ in the self-similar solution rather characterizes the accretion rate determined by the inner structure of haloes with a large value of p (number of apocentre passage). In other words, $s_{\rm best}$ is the quantity complementary to Γ_{200} and carries the information on the early-phase mass accretion history, also linked to the slope of density profile inside the splashback radius.

Note that these findings are based on an *N*-body simulation performed in an Einstein–de Sitter cosmology. One obvious question is whether these behaviours persist in standard ΛCDM cosmology or not. Although we lose strict self-similarity, recalling the fact that dynamical time-scale of halo formation is shorter than the time-scale of cosmic expansion, one expects that the similar features can be still seen, especially at the inner streams in massive haloes formed at an early time. In fact, with a slight extension of the self-similar solution, the analytical relation derived by Shi (2016) is found to describe the *N*-body haloes well in a ΛCDM cosmology (Diemer et al. 2017). In any case, a quantitative study on the radial phase-space structure of haloes in non-Einstein–de Sitter Universe is worth for further investigation, and we will address this issue in near future.

From the observational point of view, a more crucial and interesting aspect to be clarified would be the phase-space structure of subhaloes and satellite galaxies inside a halo in connection with dark matter multistream flows. These objects are known to be affected by dynamical friction, and because of this, their splashback features are systematically different from that of the dark matter (Adhikari, Dalal & Clampitt 2016; Adhikari et al. 2018). In this respect, their phase-space distribution would not exactly trace the multistream structure of dark matter. Characterizing and modelling their phase-space properties are important for confronting observations. For this purpose, a systematic study using high-resolution cosmological simulations with a large boxsize is indispensable, and it may even give a hint to probe the nature of CDM from observations.

Finally, the phase-space study of DM haloes definitely provides an important and new clue to understand the physical properties of CDM haloes. Recently, alternative to the *N*-body simulation, a more fundamental numerical method directly solving Vlasov–Poisson equations in 6D phase space is developing (Yoshikawa, Yoshida & Umemura 2013; Hahn & Angulo 2016; Sousbie & Colombi 2016). Such a technique would be certainly essential to resolve the phase-space structures deep inside the splashback, thus giving a hint to clarify the nature of cuspy density profile as well as the power-law nature of pseudo-phase-space density profile. Although this paper focuses on the phase-space structure inside the splashback radius, it is still regarded as the outer part of the halo system away from the cuspy structure. Nevertheless, an extension of the analysis to the inner phase space is straightforward. The investigation of the self-similarity and the structural properties is a crucial step towards the understanding of generic features of CDM haloes, and this is left for future work.

ACKNOWLEDGEMENTS

This work was initiated during the invitation program of Japan Society for the Promotion of Science (JSPS) Grant No. L16519. This work was granted access to HPC resources of CINES through allocations made by GENCI (Grand Equipement National de Calcul Intensif) under the allocations 2017-A0010402287 and 2018-A0030402287. Numerical computation was also carried out partly at the Yukawa Institute Computer Facility. YR thanks Shankar Agarwal for fruitful discussions about halo definitions. AT and HS would like to thank Stéphane Colombi for useful comments and references. We thank Benedikt Diemer for useful comments. This work was supported in part by MEXT/JSPS KAKENHI Grant Numbers JP15H05889, JP16H03977 (AT), JP17K14273, and JP19H00677 (TN), and Japan Science and Technology Agency CREST JPMHCR1414 (TN).

REFERENCES

Abdullah M. H., Wilson G., Klypin A., 2018, ApJ, 861, 22
Adhikari S., Dalal N., Chamberlain R. T., 2014, J. Cosmol. Astropart. Phys., 11, 019
Adhikari S., Dalal N., Clampitt J., 2016, J. Cosmol. Astropart. Phys., 2016, 022
Adhikari S., Sakstein J., Jain B., Dalal N., Li B., 2018, J. Cosmol. Astropart. Phys., 11, 033
Alard C., 2013, MNRAS, 428, 340
Bertschinger E., 1985, ApJS, 58, 39
Bertschinger E., Gelb J. M., 1991, Comput. Phys., 5, 164
Binney J., Tremaine S., 2008, Galactic Dynamics: Second Edition. Princeton University Press, Princeton, NJ
Biviano A. et al., 2013, A&A, 558, A1
Blot L., Corasaniti P. S., Alimi J.-M., Reverdy V., Rasera Y., 2015, MNRAS, 446, 1756
Blumenthal G. R., Pagels H., Primack J. R., 1982, Nature, 299, 37
Bond J. R., Szalay A. S., Turner M. S., 1982, Phys. Rev. Lett., 48, 1636
Busch P., White S. D. M., 2017, MNRAS, 470, 4767
Chang C. et al., 2018, ApJ, 864, 83
Diemer B., 2017, ApJS, 231, 5

Diemer B., Kravtsov A. V., 2014, ApJ, 789, 1
Diemer B., Mansfield P., Kravtsov A. V., More S., 2017, ApJ, 843, 140
Dolag K., Dolgov A. D., Tkachev I. I., 2013, JETP Lett., 96, 754
Drakos N. E., Taylor J. E., Benson A. J., 2017, MNRAS, 468, 2345
Fillmore J. A., Goldreich P., 1984, ApJ, 281, 1
Foreman-Mackey D., 2016, J. Open Source Softw., 24
Foreman-Mackey D., Hogg D. W., Lang D., Goodman J., 2013, PASP, 125, 306
Gunn J. E., 1977, ApJ, 218, 592
Gunn J. E., Gott J. R., III, 1972, ApJ, 176, 1
Hahn O., Angulo R. E., 2016, MNRAS, 455, 1115
Halle A., Colombi S., Peirani S., 2019, A&A, 621, A8
Henriksen R. N., Widrow L. M., 1997, Phys. Rev. Lett., 78, 3426
Jing Y. P., Suto Y., 2002, ApJ, 574, 538
Lacey C., Cole S., 1994, MNRAS, 271, 676
Lewis A., Challinor A., Lasenby A., 2000, ApJ, 538, 473
Lithwick Y., Dalal N., 2011, ApJ, 734, 100
Ludlow A. D., Navarro J. F., Springel V., Vogelsberger M., Wang J., White S. D. M., Jenkins A., Frenk C. S., 2010, MNRAS, 406, 137
MacMillan J. D., Widrow L. M., Henriksen R. N., 2006, ApJ, 653, 43
Mohayaee R., Shandarin S. F., 2006, MNRAS, 366, 1217
Mohayaee R., Colombi S., Fort B., Gavazzi R., Shandarin S., Touma J., 2006, in Mamon G. A., Combes F., Deffayet C., Fort B., eds, EAS Publ. Ser. Vol. 20, Caustics in Dark Matter Haloes. Cambridge Univ. Press, Cambridge, p. 19
More S., Diemer B., Kravtsov A. V., 2015, ApJ, 810, 36
More S. et al., 2016a, ApJ, 825, 39
More S. et al., 2016b, ApJ, 825, 39
Munari E., Biviano A., Mamon G. A., 2014, A&A, 566, A68
Navarro J. F., Frenk C. S., White S. D. M., 1996, ApJ, 462, 563
Navarro J. F. et al., 2010, MNRAS, 402, 21
Okumura T., Nishimichi T., Umetsu K., Osato K., 2018, Phys. Rev. D, 98, 023523
Peebles P. J. E., 1980, The Large-Scale Structure of the Universe. Princeton University Press, Princeton, NJ
Peebles P. J. E., 1982, ApJ, 263, L1
Planck Collaboration VI, 2018, preprint (arXiv:1807.06209)
Prunet S., Pichon C., Aubert D., Pogosyan D., Teyssier R., Gottloeber S., 2008, ApJS, 178, 179
Ryden B. S., 1993, ApJ, 418, 4
Shi X., 2016, MNRAS, 459, 3711
Sikivie P., Tkachev I. I., Wang Y., 1997, Phys. Rev. D, 56, 1863
Sousbie T., Colombi S., 2016, J. Comput. Phys., 321, 644
Suto D., Kitayama T., Osato K., Sasaki S., Suto Y., 2016a, PASJ, 68, 14
Suto D., Kitayama T., Nishimichi T., Sasaki S., Suto Y., 2016b, PASJ, 68, 97
Taylor J. E., Navarro J. F., 2001, ApJ, 563, 483
Teyssier R., 2002, A&A, 385, 337
Vogelsberger M., White S. D. M., 2011, MNRAS, 413, 1419
Vogelsberger M., White S. D. M., Mohayaee R., Springel V., 2009, MNRAS, 400, 2174
Vogelsberger M., Mohayaee R., White S. D. M., 2011, MNRAS, 414, 3044
White S. D. M., Zaritsky D., 1992, ApJ, 394, 1
Yoshikawa K., Yoshida N., Umemura M., 2013, ApJ, 762, 116
Zukin P., Bertschinger E., 2010, Phys. Rev. D, 82, 104044

This paper has been typeset from a TEX/LATEX file prepared by the author.